







Wideband and low-spurious optical waveform generator for optically addressable quantum systems manipulation and control

SACHA WELINSKI,^{1,*}  EDUARDO BEATTIE,² 
LOTHAIRE ULRICH,^{1,3} SOEREN WENGEROWSKY,² 
HUGUES DE RIEDMATTEN,^{2,4}  LOIC MORVAN,¹
AND PERRINE BERGER¹

¹Thales Research and Technology, Palaiseau 91767, France

²ICFO-Institut de Ciències Fòniques, The Barcelona Institute of Science and Technology, 08860 Castelldefels (Barcelona), Spain

³Institut Langevin, ESPCI Paris, Université PSL, CNRS, 75005 Paris, France

⁴ICREA-Institució Catalana de Recerca i Estudis Avançats, 08015 Barcelona, Spain

*sacha.welinski@thalesgroup.com

Abstract: Optical manipulation of quantum systems requires stable laser sources able to produce complex waveforms over a large frequency range. In the visible region, such waveforms can be generated using an acousto-optic modulator driven by an arbitrary waveform generator, but these suffer from a limited tuning range typically of a few tens of MHz. Visible-range electro-optic modulators are an alternative option offering a larger modulation bandwidth, however they have limited output power which drastically restricts the scalability of quantum applications. There is currently no architecture able to perform phase-stabilized waveforms over several GHz in the visible or near infrared region while providing sufficient optical power for quantum applications. Here we propose and develop a modulation and frequency conversion set-up able to deliver optical waveforms over a large frequency range, with a high spurious extinction ratio, scalable to the entire visible/near infrared region with high optical power. The optical waveforms are first generated at telecom wavelength and then converted to the emitter wavelength through a sum frequency generation process. By adapting the pump laser frequency, the optical waveforms can be tuned to interact with a broad range of optical quantum emitters or qubits such as alkali atoms, trapped ions, rare earth ions, or fluorescent defects in solid-state matrices. Using this architecture, we were able to detect and study a single erbium ion in a nanoparticle. We also generated high bandwidth signals at 606 nm, which would enable frequency multiplexing of on-demand read-out Pr³⁺:Y₂SiO₅ quantum memories.

© 2024 Optica Publishing Group under the terms of the [Optica Open Access Publishing Agreement](#)

1. Introduction

Quantum science is at a technological inflection point. Recent advances in control and readout of quantum systems have emphasized the spectacular promise of quantum information processing [1,2]. Many of these quantum systems require optical manipulation using tunable narrow linewidth lasers at visible or near infrared (IR) wavelengths [3,4], such as quantum memories based on rare earth (RE) ions [5,6] or trapped atoms [7], RE-based-spectral analyzers [8,9], alkali atom-based quantum sensors [10], or color center-based quantum nodes [1]. Some applications require optical control of the emitters over a relatively large frequency range, typically few GHz, to burn spectral features such as atomic frequency combs in the optical absorption band [11], or for coherent control of single emitters [12–14]. These manipulations require frequency tunability associated with arbitrary amplitude and/or phase modulation of optical signals over a wide bandwidth without loss of coherence. To ensure the phase and frequency stability and the

repeatability over the sequence, the laser must be controlled by a phase-locked-loop [15], which prevents frequency tuning speed faster than the GHz/ μ s range. Moreover, parasitic signals such as comb modes, sidebands from modulation, or amplified stimulated emission (ASE) can be detrimental for the targeted operation. For such applications, modulating the signals only using a tunable laser is challenging, especially when tuning across a large frequency range, over 10 GHz, with high speed, of the order of 100 GHz/ μ s [14,16].

A common solution is to run a phase-stabilized laser at constant frequency, and to modulate it externally in frequency or amplitude. However, there are currently no appropriate electro-optical modulators available with >5 GHz bandwidth in the visible region: the existing ones either show extremely low optical power handling (typically limited to few tens of mW, mainly LiNbO₃ modulators exhibiting photorefractive effects) or only phase modulation (KTP modulators). I/Q modulators enabling single sideband modulation and optical carrier suppression, with a reasonable input optical power handling, are not available in the visible spectrum. There is ongoing research towards solving this problem, especially with thin film LiNbO₃ on insulator [17,18], but power handling still remains an issue [19]. For this reason, external modulation is generally performed using acousto-optic modulators (AOMs), but these suffer from a low tuning range, speed, and bandwidth, as well as high optical losses at wavelengths where optical amplifiers can be hard to find, and a lack of versatility, with each laser source operating at a specific wavelength for a dedicated quantum system. Another potential solution is given by serrodyne techniques, which work up to roughly one GHz in continuous wave [20] but is ultimately limited by the fidelity of the high-frequency sawtooth signal, which could either be obtained from a non-linear transmission line, which would severely limit the versatility of the system, or from a high fidelity arbitrary waveform generator, which would increase the cost of the system dramatically. For femtosecond-pulsed systems, frequency shifts of up to several THz have been achieved [21], but to interface with atomic systems a narrower linewidth is needed and using a pulsed system is not an option. These limitations currently prevent the scalability and therefore the practical implementations of many quantum technologies, such as highly frequency-multiplexed optical quantum memories [22], Rydberg-based radiofrequency sensors [23], or registers of single solid-state spins, e.g. single rare-earth ions [14].

To overcome these issues, we propose in this paper to take advantage of the efficient modulation tools available at telecom wavelength in order to generate complex and tunable optical waveforms suitable for quantum protocols, combined with sum frequency generation (SFG) to convert the waveforms toward the visible range (compatible with most quantum emitters). The concept of using SFG has already been studied in [24] and has shown high dynamic range frequency conversion of two CW lasers from 1586 nm to 793 nm. Note that in comparison to second harmonic generation (SHG), which allows to convert telecom signals to the 750-790 nm-range and is usually used for rubidium spectroscopy at 780 nm [25], SFG shows many advantages: (1) Any wavelength in the visible or near IR can be accessed, provided that the right pump laser and non-linear medium are available. (2) The modulation of amplitude is proportional between the telecom and converted light (while it is quadratic for SHG). (3) No intermodulation sidebands appear when the RF modulation is multi-tone. (4) High optical powers at the converted wavelength are potentially accessible, as periodically poled lithium niobate (PPLN) waveguides have conversion efficiencies up to 100%/W/cm².

The main objective of this paper is the study of an architecture based on a I/Q modulation at telecom wavelength and a frequency conversion by SFG able to deliver optical waveforms with a high spurious extinction ratio, scalable to the entire visible/near infrared region with high optical power, over a large frequency range (up to 40 GHz if adequate RF source and non-linear medium is available). In the first section, we describe the overall set-up of the optical waveform generator. Then, we study the first building block of this architecture, which is the generation of arbitrary waveforms at telecom wavelength. We demonstrate the generation complex modulation

waveforms over a large frequency range ($> \text{GHz}$), with high extinction ratio of up to 55 dB at telecom wavelength. In a third part, we underline the advantages of this generator on a practical case: the detection of single Er^{3+} ions in Y_2O_3 nanoparticles and how to probe their optical stability. Then we preliminary demonstrate the generation of arbitrary pulses converted in the visible range, at 606 nm (the interaction wavelength of Pr^{3+} ions in Y_2SiO_5 , required for frequency multimode quantum memory preparation). We show that the extinction ratio is maintained after SFG. We finally discuss perspectives for such an optical waveform generator.

2. Description of the architecture

The architecture consists of two building blocks: a waveform generator at telecom wavelength and a frequency conversion stage to the desired wavelength, as shown in Fig. 1. The first building block includes a telecom laser, an optical I/Q modulator and an optical filter. The I/Q modulator is set-up in a single sideband (SSB) generation configuration, which means that only one 1st order harmonic constructively interferes at the modulator output. The optical carrier (0th harmonic) is also canceled. To do so, the modulator is driven by both quadratures (I and Q) of the RF modulation signal and the voltage bias must be optimized and actively stabilized. Modulators with large bandwidth of typically 40 GHz and >25 dB sideband/carrier suppression are only commercially available at the telecom wavelength (LiNbO₃ modulators). We use a tunable optical filter, also available commercially, to further filter out unwanted harmonics and therefore increase the extinction ratio of the SSB generation. The second building block performs the frequency conversion of the telecom signal to the wavelength of the quantum emitter. The converted signal is produced by SFG inside a PPLN crystal designed for such effect, by combining the telecom light with a pump laser at the appropriate wavelength in the crystal. For optical qubit control, it is crucial that the output signal exhibits high amplitude and phase stability. Several stabilization schemes can be envisaged, for example using a highly stable optical reference to which either the 1.5 μm laser source, the pump laser source, and/or the SFG signal can be actively locked. This stabilization will be investigated in the near future and is not addressed in this article.

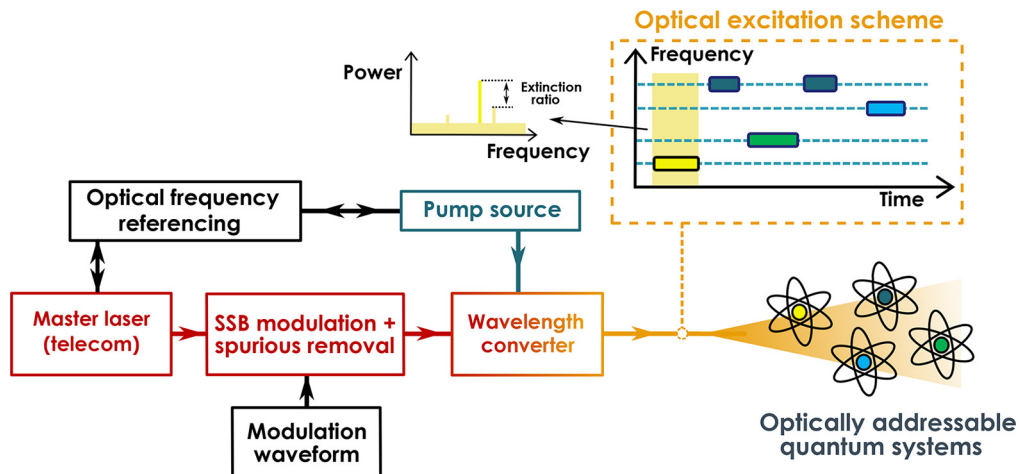


Fig. 1. Overall architecture of the optical waveform generator, described in the main text.

3. Arbitrary optical waveform generation at telecom wavelength

The experiment presented in this section explores the performance of optical signal generation at telecom wavelength. We first study a continuous wave (CW) single frequency generation, then a

complex pulse sequence. We focus on signal purity, specifically on the extinction ratio between the signal of interest and the residual harmonics remaining from imperfect SSB generation. We demonstrate the stability of the extinction over time and throughout a dynamic protocol.

3.1. Experimental set-up

The experimental set-up is described in Fig. 2. Depending on the experiment, we either use a Distributed Feedback laser (Gooch and Housego AA1406) centered at 1553 nm (193 THz) or an extended cavity diode laser (Toptica DLPro) at 1536 nm (195 THz) as the laser source, with an output power of 80 mW. The laser frequency is labeled ν_{laser} . In order to study the optical spectrum with high enough resolution, we perform a heterodyne measurement and measure the corresponding spectrum. For that, the laser line is split into two paths, a signal path and a local oscillator (LO) path. The signal path goes through an IQ optical modulator (MXIQER-LN-30 by iXblue). After the modulator, a small part of the signal is extracted to feed the bias voltage controller of the modulator, ensuring the SSB configuration, see next paragraph. A tunable optical filter (XTM 50 Yennista) is placed afterwards in order to further suppress unwanted signals, such as the carrier or high order harmonics, while preserving multi-GHz bandwidth. On the other path, which corresponds to the LO path, we place a fiber acousto-optic modulator (Gooch and Housego PM FIBER-Q) driven at $\nu_{\text{AOM}} = 80$ MHz, selecting only the first order (+1) of diffraction. The two paths are combined using a fiber beamsplitter and the light is sent to a 10 GHz bandwidth photodiode (Thorlabs RX10AF). The heterodyne signal generated is either analyzed by an Electrical Spectrum Analyser (ESA) or a high-speed oscilloscope with a sampling rate of 12 Gs/s. The I/Q modulator consists of two Mach-Zehnder modulators (MZM) placed in parallel. Under a specific bias controller configuration, depending on the chosen phase difference applied between the two MZM outputs, we can preferentially generate the harmonic +1 (that will be called H_1) or the harmonic -1 (called H_{m1}). The other harmonics are largely cancelled because of destructive interference between the different arms of the modulator. We minimize the level of 3^{rd} by operating at RF modulation power below $\text{RF } V_{\pi}$. To work in such SSB mode, three bias voltages must be set to keep an optical phase difference of π for two intensity modulators, and $\pi/2$ phase difference for their output recombination. These bias voltages are actively controlled (iXBlue modulator bias controller MBC-IQ-LAB). The I and Q signals are generated by an AWG (Keysight M8195A 8 Gs/s) and sent toward the two RF inputs of the I/Q modulator.

3.2. Results

We first send a CW RF signal to the modulator. The signal out of the photodiode is sent to an electrical spectrum analyzer (ESA). A typical spectrum is shown on Fig. 3(A), blue trace. Here the modulation frequency is $\nu_{\text{RF}} = 1.6$ GHz and the power sent to the modulator is 5 dBm. On the spectrum, we can see multiple lines corresponding to different optical beatings. The main line corresponds to the beating between H_{m1} , at $\nu_{\text{laser}} - \nu_{\text{RF}}$, and the LO, at $\nu_{\text{laser}} + \nu_{\text{AO}}$, appearing at 1.68 GHz (noted H_{m1} -LO). This line corresponds to the signal of interest. The second main line corresponds to the beating between H_1 and the LO, appearing at 1.52 GHz on the spectrum (noted H_1 -LO). The extinction ratio between H_{m1} and H_1 (ER_{H_{m1}/H_1}) is measured to be 40 dB at this RF frequency. The carrier extinction ratio with respect to the signal (ER_{H_{m1}/H_0}) is greater than 40 dB (the measurement is limited by the AOM leak, explained below). These extinction ratios strongly depend on the relative phase of the RF signal arriving on the modulator outputs, which should be as close as possible to $\pi/2$ to produce a destructive interference of one of the harmonics. This phase depends on the RF phase difference of the two signals generated by the AWG and the accumulated phase of the two different RF paths. We therefore took specific care to make the RF paths the same length, using the same RF wires and connectors, and optimized the phase difference of the I and Q signal generated by the AWG.

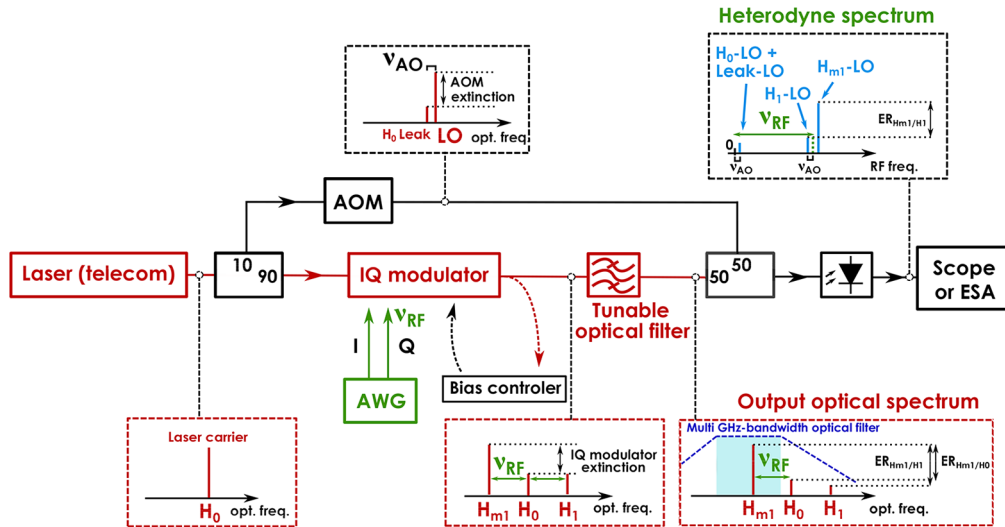


Fig. 2. Heterodyne experimental set up for characterizing the single sideband (SSB) modulation, see details in main text. Insets : optical & heterodyne spectra at different positions in the experiment. The turquoise region corresponds to the signal generation bandwidth delimited by the optical filter. Red : main optical path, Green : RF signal, Black : characterization tools and electronics.

Figure 3(B) shows the extinction ratios with and without the optical filter versus modulation frequency. Without filter, we see that ER_{H_{m1}/H_1} stays relatively constant, around 25 dB, which is in agreement with the I/Q modulator specifications. The blue curve shows ER_{H_{m1}/H_1} with the tunable optical filter of the experiment, exhibiting a 6.4 dB/GHz cutoff slope. We placed the optical filter so that the 3 dB-edge was 1 GHz away from the carrier (see corresponding inset of Fig. 2). By doing this, the symmetric harmonic with respect to the carrier laser frequency was suppressed even more as the RF frequency increased. We can see that ER_{H_{m1}/H_1} increases with modulation frequency, and closely follows the filter cutoff specification of 6.4 dB/GHz. The highest extinction ratio was measured to be 55 dB for a modulation frequency of 3.5 GHz, corresponding to the highest available using our AWG. Using a steeper tunable filter (i.e. the Alnair-labs CVF-300) would further increase the extinction ratio with respect to RF frequency, as shown with the turquoise dashed curve. There are other small signals to be seen in the spectrum: the signal at 3.28 GHz corresponds to a beating between the remaining second order modulation H_{m2} and the LO; the signal at 80 MHz is a superposition of two signals with a relative power of -95.3 dB (blue trace on Fig. 3(A)) : the AOM 1st order beating with the residual 0th order (noted AOM leak, the AOM being specified with 50 dB extinction) and remaining carrier H_0 beating with the LO (noted H_0 -LO). The AOM leak alone is visible when the signal line is blocked, with a relative power of -98 dB when signal line is blocked (red trace). We can therefore estimate the H_0 -LO signal has a relative power of -98.6 dB.

We then aimed to generate complex arbitrary optical waveforms which could be used to coherently control optical quantum emitters. We chose to generate frequency chirped secant-hyperbolic pulses (HSH pulses [26]), known to perform efficient population inversions over a specific optical bandwidth. These pulses can yield uniform excitation over a defined bandwidth with a very sharp cut-off at the edges, and are used as control pulses for spin wave quantum memories [27]. Such pulses are extremely difficult to create over a large bandwidth using AOMs. Here we show that we can efficiently generate such HSH pulses over a span of several GHz, while keeping a good sideband and carrier extinction. In order to measure dynamic signals, we no

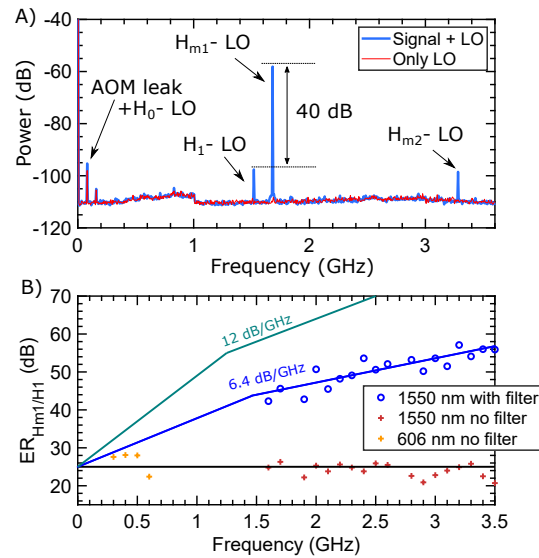


Fig. 3. A. Typical electrical spectrum of the heterodyne beating between the signal and the LO on the photodiode ($\nu_{RF} = 1.6$ GHz), with optical filter. B. Variations of ER_{H_{m1}/H_1} with respect to modulation frequency: without (black curve) and with (blue curve) optical filter (with a cutoff slope of 6.4 dB/GHz). Turquoise curve: better commercial tunable filter with a cutoff slope of 12 dB/GHz (*Alnair-labs company*). Experimental points with/without filter at 1550 nm and 606 nm are shown, see inserted legend.

longer use an ESA and we instead use a high-speed oscilloscope (6 GHz analog bandwidth) and directly digitize a timeframe of the electrical signal generated by the photodiode. We then do a spectral analysis of the signals and measure the extinction ratios at different temporal regions of the waveform. We generate a sequence of HSH pulses, in which each pulse is centered at a different frequency and has the same amplitude. The pulses have a duration of 10 μ s and a frequency chirp of 100 kHz. The delay between two pulses is 20 μ s and the edge duration is 0.5 μ s. Figure 4 shows a sequence with frequencies centered around 1.6 GHz and 2.6 GHz. A first measurement is taken just after the sequence starts and another one a few minutes later. By comparing the two, we can study the long-term stability of the extinction, and therefore the bias control stability of the modulator. In this case, the two measurements gave similar results, which means that such sequence does not destabilize the bias voltage control. Figure 4 shows a measurement a few minutes after the start of the sequence. We can see on 4(A) the temporal signal acquired by the oscilloscope. We select two temporal regions (red and green) corresponding to two different pulses at modulation frequency of respectively 1.6 GHz and 2.6 GHz. The spectrum corresponding to those regions are displayed in 4(C) and 4(D). For the 1.6 GHz HSH pulse, the beating signal H_1 -LO (resp. H_{m1} -LO) appears at 1.6 GHz - 80 MHz (resp. + 80 MHz). For the 2.6 GHz HSH pulse, H_1 -LO (resp. H_{m1} -LO) appears at 2.6 GHz - 80 MHz (resp. + 80 MHz). We measure respectively ER_{H_{m1}/H_1} to be 37 dB and 41 dB, which is the same as it is right after the sequence starts. This demonstrates the high rejection we are able to attain with such an architecture. The signals appearing at 1.6 GHz and 2.6 GHz, labeled H_{m1} - H_0 corresponds to the beating signal of H_{m1} with remaining H_0 .

We note that ER_{H_{m1}/H_1} is slightly lower than in the CW regime (Fig. 3(B)). This could be due to a less efficient control of the modulator bias in a dynamic regime. The central peaks to be seen at 1.6 GHz in 3(C) and 2.6 GHz in 3(D) correspond to the beating between H_{m1} and H_0 . The small oscillations with 30 MHz period at the foot of the main signal beating correspond to

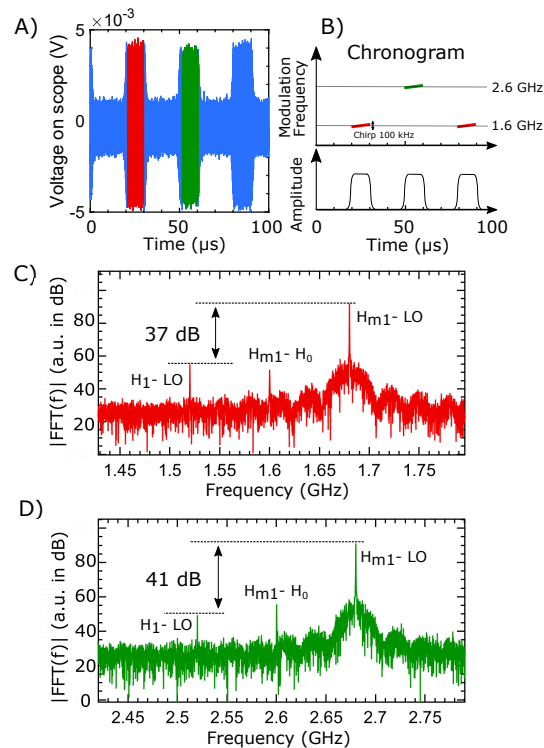


Fig. 4. A. HSH pulses of duration $10 \mu\text{s}$, inter-pulses delay $20 \mu\text{s}$, edge $0.5 \mu\text{s}$, chirp 100 kHz , at 1.6 GHz and 2.6 GHz , and same amplitude as explicated in the chronograms shown in B. C and D. FFT spectra for a HSH pulse at 1.6 GHz and 2.6 GHz , a few minutes after sequence started.

the phase noise of the DFB laser, filtered by the 7 m measurement interferometer, and could be reduced using a lower phase noise telecom laser, such as an Integrated Tunable Laser Assembly (ITLA). We also observe a drop of the extinction ratio when the pulse duty cycle is increased: the modulator does not work on SSB configuration anymore (see Supplementary materials). This happens when the RF signals are switched on and off over timescales between $30 \mu\text{s}$ and $100 \mu\text{s}$. Indeed, changes of RF power can induce thermal fluctuations, and therefore change the relative optical phase in the different paths of the modulator, destabilizing the feedback bias voltage control loop. We solved this issue by introducing filling pulses in the modulation sequence, which continually apply RF power on the modulator and therefore maintain a constant heating on the timescale of the bias feedback loop (see Supplementary materials). The frequency of the filling pulses has to be set so that the optical signal is not resonant with any quantum emitters, and does not disturb the quantum system. We verified that using this method the extinction ratio is preserved, while it rapidly drops without filling pulses. In this experiment, the generation of filling pulses by the AWG limits the bandwidth that can be used to generate the useful signals. However, this is not a fundamental limitation, since other active bias stabilization schemes could be considered to be resilient to the required impulse modulation signals [28].

4. Application case: single rare-earth ion spectroscopy

Single quantum emitters are useful for many quantum technologies, such as single photon sources [29] or quantum networking via spin-photon entanglement [1,30]. In particular, single REs are of interest due to their exceptionally narrow optical lines—down to a few tens of kHz [31]—and

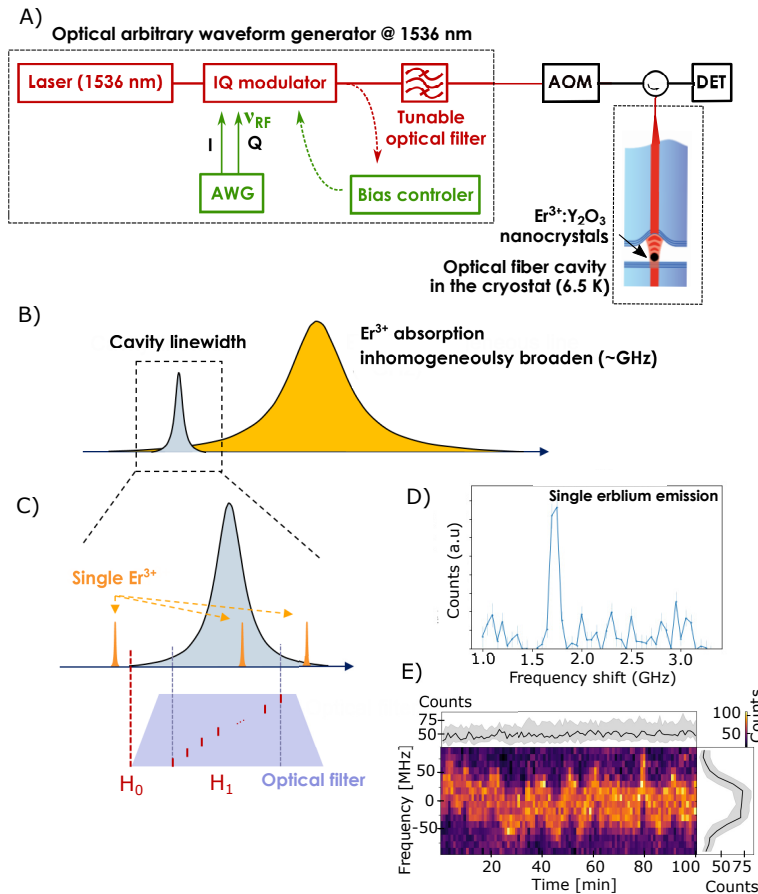


Fig. 5. A. Scheme of the experimental set-up. The I/Q modulator followed by the optical filter enables large frequency scan without any drift. The temporal pulses are done with the AOM. B. Cavity linewidth with respect to the erbium optical inhomogeneous lines. C. Zoom in frequency with respect to B. D. Optical absorption line of a single erbium ion. The laser frequency is swept through the cavity linewidth. E. Photoluminescence spectra over time showing the spectral diffusion of the optical absorption line.

these ions have demonstrated promising properties for quantum applications when measured as an ensemble at cryogenic temperature [32,33]. However, the detection of single REs requires extremely stable lasers with a linewidth at least as narrow as the optical transition. The laser must therefore be locked to a high finesse reference cavity, but this restricts tunability and prevents large scans over the inhomogeneous linewidth, which can be a few GHz wide [34]. A series of acousto-optic modulators can shift the frequency over a limited range of a few hundred MHz, which is not sufficient to perform GHz-scale scans. Here we show that the modulation architecture presented above makes it possible to perform such measurements and detect single erbium ions in Y_2O_3 nanoparticles. The full report of this experiment is available at Ref. [35].

The emission of the REs is Purcell enhanced by placing the nanoparticles inside an optical cavity, which consists of a macroscopic planar mirror and the tip of an optical fiber which is machined with a concave profile and mirror coated. This cavity is placed inside a closed-cycle cryostat and cooled down to 6.5 K. Optical excitation pulses are sent into the cavity via the fiber, and ions emission is collected through the same fiber and sent to single photon detectors.

Figure 5(A) shows the experimental set-up. The cavity resonance is tuned to the edge of the erbium absorption line (Fig. 5(B)) in order to reduce the spectral density of interacting ions, which enables the detection of distinctly single emitters. The excitation laser is an external cavity diode laser centered at 1536 nm. Without stabilization, the intrinsic linewidth of the laser is a few hundreds of kHz and experiences a slow drift over time. A Pound-Drever-Hall lock to a high finesse cavity results in a linewidth reduction down to the kHz level and a drift correction.

As a first step, wide scans (over the linewidth of the fiber cavity in the cryostat, which is close to 0.5 GHz (see 5(C)), were performed by changing the modulation frequency generated by the AWG. This frequency change was monitored by the main experiment in order to be synchronized with the photoluminescence collection. Figure 5(D) shows an example of a photoluminescence spectrum shows the emission of a single erbium ion. The typical linewidth of the single ion measured is typically tens of MHz. Hanbury-Brown–Twiss measurements were performed to demonstrate the antibunching correlation signal, which is a characteristic signature of single emitters. Fine spectra over the single ion lines were able to be measured without any laser drift even over long times, making it possible to study the spectral diffusion of these optical lines. In Fig. 5(E) continuous frequency scans over a single ion optical line were performed over 100 minutes; we can see that its resonance fluctuates over a 50 MHz range due to environmental perturbations. We can also note a stable emission rate, with no blinking over time. While in this experiment our modulator was only used to provide fixed frequency offsets, its ability to produce arbitrary waveforms over a GHz-range bandwidth is a key technological requirement for the control of qubits based on single REs as described in Ref. [14], and thus our work represents a milestone towards RE quantum computing.

5. Arbitrary optical waveform generation at visible wavelength

We saw in the last sections that we can generate wideband complex optical waveforms with remarkable extinction ratio at telecom wavelength thanks to the technological maturity of electro-optic technologies in this band. Such architecture cannot be implemented at visible wavelength due to the lower performance of optical components. However, the telecom optical waveform can be converted to visible wavelength using a non-linear medium.

Here we chose to generate the optical waveform at 606 nm, which corresponds to the wavelength used to control optical quantum memories based on praseodymium ions (Pr^{3+} doped Y_2SiO_5). The telecom signal undergoing the optical waveform is combined with a 994 nm laser (pump laser) beam into a 4.8 cm-long PPLN waveguide (see Fig. 6). The poling period of 10.2 μm ensures quasi-phase matching for the sum frequency generation (SFG) between those two frequencies, resulting in light at 606 nm. Using a pump power of 120 mW at 994 nm, and 47 mW at 1552 nm, we obtained 90 mW of optical power at 606 nm. This corresponds to a device conversion efficiency of 75%. We measured the beating between the SFG-generated 606 nm beam and a reference laser at 606 nm (494.7254 THz) on a fast photodiode (Coherent EOT4000, 10 GHz bandwidth) : the reference laser acts as a local oscillator; it is stabilized on a vacuum cavity, and emits exactly at the frequency of the Pr^{3+} ions. The carrier frequency of the telecom laser is tuned to generate SFG light 60 MHz apart from reference laser.

We generate a sequence of HSH pulses using the I/Q modulator. Each pulse has a duration of 10 μs and the frequency chirp bandwidth is 100 kHz. The delay between two pulses is 100 ns and the edge duration is 0.5 μs . The central frequency jumps by 100 MHz between each pulse, and cycles between 300 MHz and 600 MHz. The modulation frequency was limited by the available ADC sampling rate in this experiment, and modulation up to several GHz would have been possible without this limitation. The temporal waveform and corresponding Fourier spectra are shown in Fig. 7. In all the spectra, the beating signal corresponding to H0-LO is below the noise floor and cannot be seen, meaning that the carrier laser is largely suppressed. We clearly see the beating notes H_1 -LO (resp. H_{m1} -LO) at $\nu_{\text{RF}} - 60$ MHz (resp. $+ 60$ MHz). The

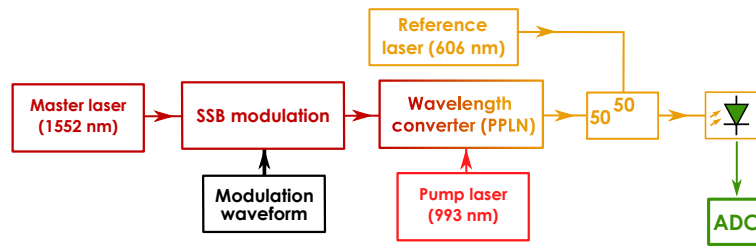


Fig. 6. Heterodyne experimental set-up for characterizing the optical waveform frequency shifted to 606 nm. The reference laser is shifted by 60 MHz with respect to the wavelength-converted-sideband.

extinction ratio $ER_{Hm1/H1}$ is measured to be more than 25 dB, except for the highest modulation frequency. These measurements were performed without any photonics filter. The extinction ratios measured here are similar to those measured at telecom wavelength (see Fig. 3)), which indicates that the frequency conversion stage did not degrade the spectral purity of the optical waveform, and that, with the optical filter, rejection of more than 50 dB could also be achieved at the converted wavelength.

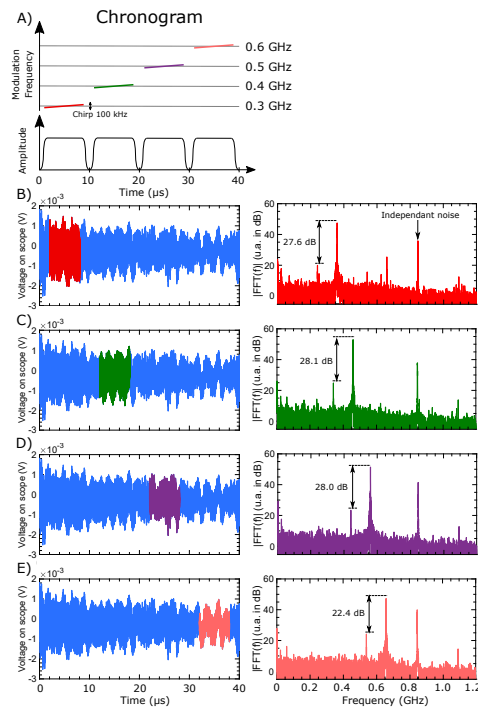


Fig. 7. A. Chronograms of HSH pulses at 606 nm, [300 400 500 600] MHz, duration 10 μ s, delay 100 ns, chirp 100 kHz, edge 0.5 μ s BCDE) Temporal acquisition and Fourier spectra of a HSH pulse, at B : 0.3 GHz C : 0.4 GHz D : 0.5 GHz E : 0.6 GHz after a few minutes after sequence started.

6. Discussion

Through the generation of a complex optical waveform at 606 nm we have demonstrated the versatility of our architecture, that is able to reach any visible or near IR wavelength, provided that a frequency-stabilized pump laser and PPLN crystal are available. This approach is particularly interesting for wavelengths where modulation tools are inefficient or reduce the amount of optical power available. In comparison, modulation tools at telecom wavelength show very small optical losses and can generally hold much higher power. Here we show that complex optical signals with at least 90 mW of optical power can be achieved. We have demonstrated the modulation of an optical signal up to 3.5 GHz, which could be extended directly to 40 GHz by using for example digital generation combined with agile RF signal generator: digital generation combined with agile RF upconversion to create optical excitation schemes such as illustrated in Fig. 1. The phase matching bandwidth of the PPLN can also limit the generated signal bandwidth. In our case, we measured a 3 dB bandwidth on the sum frequency efficiency of 25 GHz around the wavelength maximizing the phase matching. It would be possible to achieve a phase matching bandwidth of 40 GHz by using a shorter PPLN crystal than the one we have used. There are many optically addressable quantum systems that would benefit from such architecture, including but not limited to optical clocks based on neutral Yb, Sr or Cs cold atoms [36,37], rubidium and cesium Rydberg RF sensors [10,38] and Eu^{3+} , Pr^{3+} , Tm^{3+} , Yb^{3+} doped materials for spectrally multiplexed optical quantum memories [39–42] or RF wideband spectral analysis [8,9]. We believe this architecture can also be useful for classical optical applications in the visible spectrum where frequency agility is required while keeping a narrow linewidth laser and frequency stability, such as fiber optic sensors or LIDARs [43,44]. Two important parameters for all these applications are the laser linewidth and the frequency stability. In our architecture, we expect the noise of the two lasers to add incoherently. One could imagine either using two stable lasers, or frequency locking the sum frequency signal on a reference and feeding back on one of the two lasers. Another important parameter is the signal to noise ratio. In this study, a focus was made on the characterization of spurious generated by the IQ modulation and their suppression. For multi-tone signals, intermodulations will appear due to the modulator intrinsic non-linearity whatever the wavelength operation of the modulator [45–47]. Such distortions could be taken into account in the definition of the arbitrary waveforms required for quantum protocol. However, there might also be spurious and noise generated in the nonlinear medium, such as cascaded three wave-mixing processes, even if a low spurious level has been characterized in [24] for multi-tone signals and noises such as USPDC (up-conversion spontaneous parametric down-conversion) where a pump photon is split by parametric fluorescence due to random quasi phase matching before being efficiently up-converted [48,49]. If extremely large modulation bandwidths were required—larger than the 40 GHz potentially offered by our system—then several modulation channels could be used and combined before frequency conversion. An optical frequency comb combined with an optical demultiplexer could be used to send different comb lines to the different modulation channels, as it is already done in many microwave photonics experiments [50]. In terms of scalability, the recent development of integrated lithium niobate on insulator (LNoI) platforms might provide in the near future on-chip modulators co-integrated with non-linear frequency conversion functions [51]. The architectures presented in this work could be realized on chip, leading to a great reduction in volume of components required for atomic and molecular physics experiments.

7. Conclusion

In this work, we have presented an architecture capable of generating complex optical waveforms to manipulate and control optically addressable quantum systems in the visible and near IR region based on the generation of optical waveforms at the telecom wavelength followed by

frequency transfer through sum frequency conversion. We demonstrated the production of complex optical waveforms with a high spurious extinction of 40–55 dB at telecom wavelength over a bandwidth of 3.5 GHz. The extinction could be further improved to the 60–80 dB range by using other currently available optical filters. Furthermore, the bandwidth was limited by our AWG and the PPLN, and with a different RF source (for example combining digital generation combined with agile RF upconversion) and nonlinear crystal it could be pushed close to the 40 GHz bandwidth of our I/Q modulator. Using our set-up, we were able to detect single Er^{3+} ions in Y_2O_3 nanoparticles and probe their optical stability in time. We also generated optical waveforms able to control multimode quantum memories based on Pr^{3+} ions in Y_2SiO_5 at 606 nm, a wavelength where no high bandwidth modulators are available. Our work paves the way toward efficient, wideband, and low noise optical waveform generation, and thus enables the control and manipulation of a wide variety of optically addressable quantum systems.

8. Supplementary materials

We observe that the long term stability of the extinction ratio depends on the period of the train pulses. Here we show two examples: The first is a train of 10 μs pulses with a 20 μs delay between each pulse (Fig. 8). The second one is the same sequence with two missing pulses every two pulses. There is therefore a delay of 80 μs between two pulse trains. On the first example, the extinction ratio $\text{ER}_{\text{Hm1}/\text{H1}}$ does not change in time, and stays around 25 dB (note that we do not use an optical filter to increase $\text{ER}_{\text{Hm1}/\text{H1}}$ in this experiment). On the second example (Fig. 9), where there is a 80 μs delay between pulse trains, we see a drop of $\text{ER}_{\text{Hm1}/\text{H1}}$, from 25 dB after the sequence starts to 7 dB after a few minutes. This means that the modulator does not work on SSB configuration anymore. This is certainly due to the fact that rapid changes in the

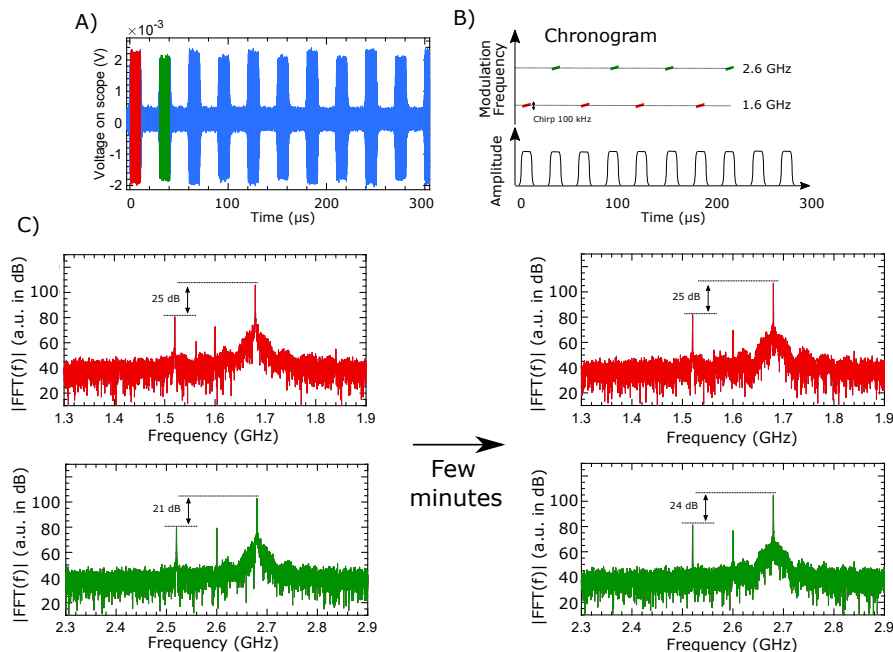


Fig. 8. A. Train of HSH pulses of duration 10 μs , inter-pulses delay 20 μs , edge 0.5 μs , chirp 100 kHz, at 1.6 GHz and 2.6 GHz, and same amplitude as illustrated in the chronograms shown in B. There is no optical filter. C and D. FFT spectra for a HSH pulse at 1.6 GHz and 2.6 GHz, just after starting the sequence and a few minutes after sequence started.

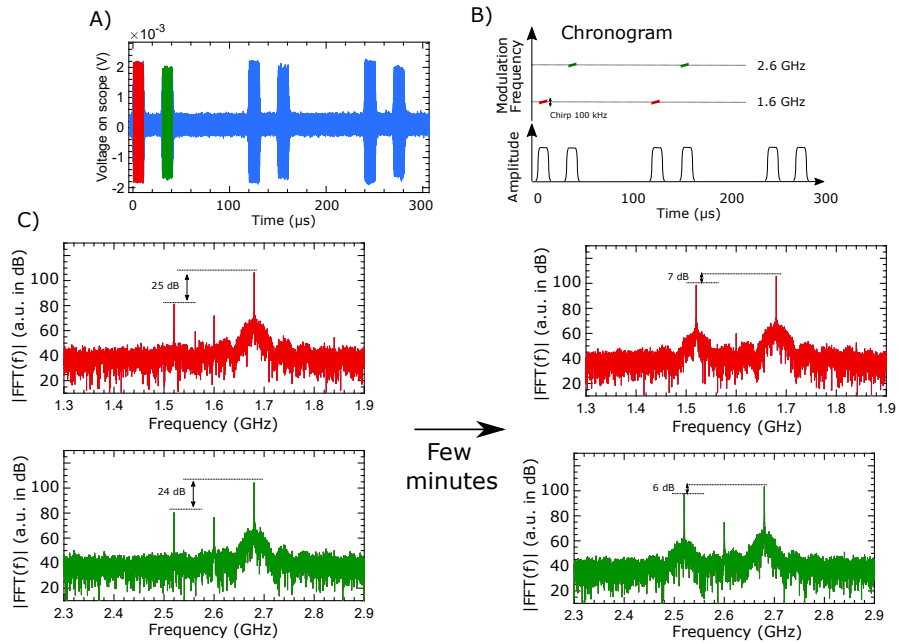


Fig. 9. A. Train of two HSH pulses of duration 10 μs , inter-pulses delay 20 μs , delay between pulse trains of 80 μs , edge 0.5 μs , chirp 100 kHz, at 1.6 GHz and 2.6 GHz, and same amplitude as illustrated in the chronograms shown in B. There is no optical filter. C and D. FFT spectra for a HSH pulse at 1.6 GHz and 2.6 GHz, just after starting the sequence and a few minutes after sequence started.

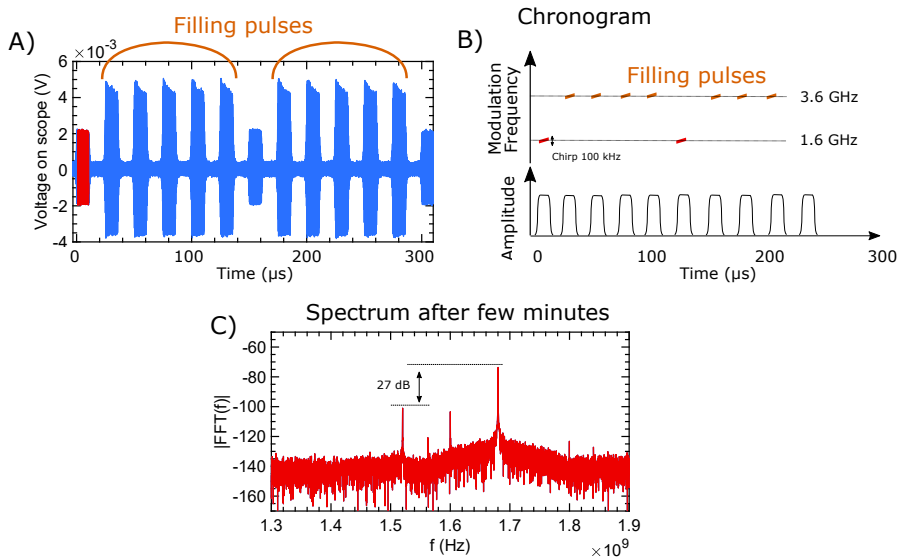


Fig. 10. A. Train of two HSH pulses of duration 10 μs , inter-pulses delay 150 μs , edge 0.5 μs , chirp 100 kHz, at 1.6 GHz and filling pulses centered at 3.6 GHz as illustrated in the chronograms shown in B. There is no optical filter. C. FFT spectrum for a HSH pulse at 1.6 GHz a few minutes after sequence started.

modulation RF signal can induce fluctuations of the relative optical phase in the different paths of the modulator — for example due to thermal effects — which can periodically perturb the feedback bias voltage control loop.

We solved this bias stability issue using filling pulses. The purpose of these filling pulses is to maintain a high rate of RF pulses in the modulator, and therefore a constant heat load. We chose the filling pulses to have modulation frequency much higher than the control pulses, so that they are not resonant with any optical emitters, and therefore do not disturb the quantum system. Figure 10 shows an example of sequence with filling pulses. After a few minutes, the extinction ratio is preserved ($ER_{Hm1/H1} = 27$ dB, meaning the SSB modulation is effective).

Funding. HORIZON EUROPE Excellent Science (820391, SQUARE); HORIZON EUROPE Digital, Industry and Space (101102140, Quantum Internet Alliance - Phase1).

Acknowledgements. We thank Romain Demur and Arnaud Grisard for the fruitful discussions on nonlinear frequency conversion.

Disclosures. The authors declare no conflicts of interest.

Data availability. Data underlying the results presented in this paper are not publicly available at this time but may be obtained from the authors upon reasonable request.

References

1. M. Pompili, S. L. N. Hermans, S. Baier, *et al.*, “Realization of a multi-node quantum network of remote solid-state qubits,” *Science* **372**(6539), 259–264 (2021).
2. A. Ruskuc, C.-J. Wu, J. Rochman, *et al.*, “Nuclear spin-wave quantum register for a solid-state qubit,” *Nature* **602**(7897), 408–413 (2022).
3. M. Atatüre, D. Englund, N. Vamivakas, *et al.*, “Material platforms for spin-based photonic quantum technologies,” *Nat. Rev. Mater.* **3**(5), 38–51 (2018).
4. D. D. Awschalom, R. Hanson, J. Wrachtrup, *et al.*, “Quantum technologies with optically interfaced solid-state spins,” *Nat. Photonics* **12**(9), 516–527 (2018).
5. C. Clausen, I. Usmani, F. Bussières, *et al.*, “Quantum Storage of Photonic Entanglement in a Crystal,” *Nature* **469**(7331), 508–511 (2011).
6. C. Simon, M. Afzelius, J. Appel, *et al.*, “Quantum memories,” *Eur. Phys. J. D* **58**(1), 1–22 (2010).
7. M. Cao, F. Hoffet, S. Qiu, *et al.*, “Efficient reversible entanglement transfer between light and quantum memories,” *Optica* **7**(10), 1440 (2020).
8. P. Berger, Y. Attal, M. Schwarz, *et al.*, “RF Spectrum Analyzer for Pulsed Signals: Ultra-Wide Instantaneous Bandwidth, High Sensitivity, and High Time-Resolution,” *J. Lightwave Technol.* **34**(20), 4658–4663 (2016).
9. W. R. Babbitt, “Microwave photonic processing with spatial-spectral holographic materials,” in *Optical, Opto-Atomic, and Entanglement-Enhanced Precision Metrology II*, S. M. Shahriar and J. Scheuer, eds. (SPIE, San Francisco, United States, 2020), p. 128.
10. C. L. Holloway, J. A. Gordon, S. Jefferts, *et al.*, “Broadband Rydberg Atom-Based Electric-Field Probe for SI-Traceable, Self-Calibrated Measurements,” *IEEE Trans. Antennas Propag.* **62**(12), 6169–6182 (2014).
11. M. Afzelius, C. Simon, H. De Riedmatten, *et al.*, “Multimode quantum memory based on atomic frequency combs,” *Phys. Rev. A* **79**(5), 052329 (2009).
12. M. Raha, S. Chen, C. M. Phenicie, *et al.*, “Optical quantum nondemolition measurement of a single rare earth ion qubit,” *Nat. Commun.* **11**(1), 1605 (2020).
13. S. Chen, M. Raha, C. Phenicie, *et al.*, “Parallel single-shot measurement and coherent control of solid-state spins below the diffraction limit,” *Science* **370**(6516), 592–595 (2020).
14. A. Kinos, D. Hunger, R. Kolesov, *et al.*, “Roadmap for Rare-earth Quantum Computing,” *arXiv*, arXiv:2103.15743v1 (2021).
15. G. Kervella, J. Maxin, M. Faugeron, *et al.*, “Laser sources for microwave to millimeter-wave applications [Invited],” *Photonics Res.* **2**(4), B70 (2014).
16. A. Kinos, L. Rippe, D. Serrano, *et al.*, “High-connectivity quantum processor nodes using single-ion qubits in rare-earth-ion-doped crystals,” *Phys. Rev. A* **105**(3), 032603 (2022).
17. H. Fukuzawa, J. Yoshinari, H. Hara, *et al.*, “Visible light modulator by sputter-deposited lithium niobate,” *AIP Adv.* **12**(6), 065029 (2022).
18. D. Pohl, J. Kellner, F. Kaufmann, *et al.*, “High-Bandwidth Lithium Niobate Electro-Optic Modulator at Visible-Near-Infrared Wavelengths,” in *European Conference on Optical Communication (ECOC) 2022 (2022)*, paper Tu4E.1, (Optica Publishing Group, 2022), p. Tu4E.1.
19. S. Xue, Z. Shi, J. Ling, *et al.*, “Full-spectrum visible electro-optic modulator,” *Optica* **10**(1), 125 (2023).
20. D. M. S. Johnson, J. M. Hogan, S.-w. Chiow, *et al.*, “Broadband optical serrodyne frequency shifting,” *Opt. Lett.* **35**(5), 745 (2010).

21. P. Balla, H. Tünnermann, S. H. Salman, *et al.*, “Ultrafast serrodyne optical frequency translator,” *Nat. Photonics* **17**(2), 187–192 (2023).
22. A. Seri, D. Lago-Rivera, A. Lenhard, *et al.*, “Quantum Storage of Frequency-Multiplexed Heralded Single Photons,” *Phys. Rev. Lett.* **123**(8), 080502 (2019).
23. D. H. Meyer, Z. A. Castillo, K. C. Cox, *et al.*, “Assessment of Rydberg Atoms for Wideband Electric Field Sensing,” *J. Phys. B: At., Mol. Opt. Phys.* **53**(3), 034001 (2020).
24. R. J. Barbour, T. Brewer, and Z. W. Barber, “High power and high SFDR frequency conversion using sum frequency generation in KTP waveguides,” *Opt. Lett.* **41**(15), 3639 (2016).
25. A. Kodigala, M. Gehl, G. W. Hoth, *et al.*, “Silicon Photonic Single-Sideband Generation with Dual-Parallel Mach-Zehnder Modulators for Atom Interferometry Applications,” Tech. Rep. [arXiv](https://arxiv.org/abs/2204.12537), arXiv:2204.12537, (2022).
26. M. Tian, T. Chang, K. D. Merkel, *et al.*, “Reconfiguration of spectral absorption features using a frequency-chirped laser pulse,” *Appl. Opt.* **50**(36), 6548 (2011).
27. J. V. Rakonjac, G. Corrielli, D. Lago-Rivera, *et al.*, “Storage and analysis of light-matter entanglement in a fibre-integrated system,” [arXiv](https://arxiv.org/abs/2201.03361), arXiv:2201.03361 [quant-ph] (2022).
28. M. Zhang, Y. Li, X. Ding, *et al.*, “Review of Bias Point Stabilization Methods for IQ Modulator,” in *Communications, Signal Processing, and Systems*, vol. 874 Q. Liang, W. Wang, X. Liu, *et al.*, eds. (Springer Nature Singapore, Singapore, 2023), pp. 172–179.
29. M. D. Eisaman, J. Fan, A. Migdall, *et al.*, “Invited Review Article: Single-photon sources and detectors,” *Rev. Sci. Instrum.* **82**(7), 071101 (2011).
30. A. Reiserer, N. Kalb, G. Rempe, *et al.*, “A quantum gate between a flying optical photon and a single trapped atom,” *Nature* **508**(7495), 237–240 (2014).
31. J. M. Kindem, A. Ruskuc, J. G. Bartholomew, *et al.*, “Control and single-shot readout of an ion embedded in a nanophotonic cavity,” *Nature* (2020).
32. D. Serrano, J. Karlsson, A. Fossati, *et al.*, “All-optical control of long-lived nuclear spins in rare-earth doped nanoparticles,” *Nature Communications* pp. 1–7 (2017).
33. A. Fossati, S. Liu, J. Karlsson, *et al.*, “A Frequency-Multiplexed Coherent Electro-Optic Memory in Rare Earth Doped Nanoparticles,” *Nano Lett.* **20**(10), 7087–7093 (2020).
34. A. M. Dibos, M. Raha, C. M. Phenicie, *et al.*, “Atomic Source of Single Photons in the Telecom Band,” *Phys. Rev. Lett.* **120**(24), 243601 (2018).
35. C. Deshmukh, E. Beattie, B. Casabone, *et al.*, “Detection of single ions in a nanoparticle coupled to a fiber cavity,” *Optica* **10**(10), 1339 (2023).
36. M. Pizzocaro, P. Thoumany, B. Rauf, *et al.*, “Absolute frequency measurement of the $^1S_0 - ^3P_0$ transition of ^{171}Yb ,” *Metrologia* **54**(1), 102–112 (2017).
37. P. Barbieri, C. Clivati, M. Pizzocaro, *et al.*, “Spectral purity transfer with 5×10^{-17} instability at 1 s using a multibranch Er: fiber frequency comb,” *Metrologia* **56**(4), 045008 (2019).
38. M. Jing, Y. Hu, J. Ma, *et al.*, “Quantum superhet based on microwave-dressed Rydberg atoms,” *Nat. Phys.* **16**(9), 911–915 (2020).
39. A. Ortu, A. Holzäpfel, J. Etesse, *et al.*, “Storage of photonic time-bin qubits for up to 20 ms in a rare-earth doped crystal,” *npj Quantum Inf.* **8**(1), 29 (2022).
40. D. Lago-Rivera, S. Grandi, J. V. Rakonjac, *et al.*, “Telecom-heralded entanglement between multimode solid-state quantum memories,” *Nature* **594**(7861), 37–40 (2021).
41. W. Tittel, M. Afzelius, T. Chanelière, *et al.*, “Photon-echo quantum memory in solid state systems,” *Laser Photonics Rev.* **4**(2), 244–267 (2010).
42. M. Businger, A. Tiranov, K. T. Kaczmarek, *et al.*, “Optical Spin-Wave Storage in a Solid-State Hybridized Electron-Nuclear Spin Ensemble,” *Phys. Rev. Lett.* **124**(5), 053606 (2020).
43. A. G. Leal-Junior and C. Marques, “Diaphragm-Embedded Optical Fiber Sensors: A Review and Tutorial,” *IEEE Sens. J.* **21**(11), 12719–12733 (2021).
44. B. Cochenour, L. Mullen, and J. Muth, “Modulated pulse laser with pseudorandom coding capabilities for underwater ranging, detection, and imaging,” *Appl. Opt.* **50**(33), 6168 (2011).
45. D. A. I. Marpaung, “High dynamic range analog photonic links: design and implementation,” Ph.D. thesis (2009).
46. E. Ackerman, S. Wanuga, D. Kasemset, *et al.*, “Maximum dynamic range operation of a microwave external modulation fiber-optic link,” *IEEE Trans. Microwave Theory Tech.* **41**(8), 1299–1306 (1993).
47. Y. Shi, L. Yan, and A. E. Willner, “High-speed electrooptic modulator characterization using optical spectrum analysis,” *J. Lightwave Technol.* **21**(10), 2358–2367 (2003).
48. L. Meng, A. Padhye, C. Pedersen, *et al.*, “SHG (532 nm)-induced spontaneous parametric downconversion noise in 1064-nm-pumped IR upconversion detectors,” *Opt. Lett.* **44**(7), 1670 (2019).
49. J. S. Pelc, “Frequency Conversion of Single Photons: Physics, Devices, and Applications,” (2012).
50. D. Fang, A. Zazzi, J. Muller, *et al.*, “Optical Arbitrary Waveform Measurement (OAWM) Using Silicon Photonic Slicing Filters,” *J. Lightwave Technol.* **40**(6), 1705–1717 (2022).
51. S. Saravi, T. Pertsch, and F. Setzpfandt, “Lithium Niobate on Insulator: An Emerging Platform for Integrated Quantum Photonics,” *Adv. Opt. Mater.* **9**(22), 2100789 (2021).